Quantum computing and quantum optics with recoiled free electrons

Maxim Sirotin [1,2,3,4,*] Andrei Rasputnyi [1,2,†] Tomáš Chlouba [1,‡] Roy Shiloh [1,5,§] and Peter Hommelhoff [1,6,‖]

[1]*Department of Physics, Friedrich-Alexander-Universität Erlangen-Nürnberg, 91058 Erlangen, Germany*

[2]*Max Planck Institute for the Science of Light, 91058 Erlangen, Germany*

[3]*Department of Physics, Harvard University, Cambridge, Massachusetts 02138, USA*

[4]*Research Laboratory of Electronics, Massachusetts Institute of Technology (MIT), Cambridge, Massachusetts 02139, USA*

[5]*Institute of Applied Physics, Hebrew University of Jerusalem, Jerusalem 9190401, Israel*

[6]*Faculty of Physics, Ludwig-Maximlians-Universität München, 80799 München, Germany*

(Received 21 May 2026; accepted 9 October 2026; published 2 November 2026)

Coherent interactions between free electrons and optical fields offer a promising route to quantum control, nonclassical state generation, and programmable quantum dynamics. At kiloelectron-volt electron energies, the emission or absorption of optical photons produces appreciable quantum recoil, resolving the electron into a discrete and controllable energy ladder. Starting from relativistic quantum electrodynamics, we derive an exact recoil-resolved interaction Hamiltonian in a traveling-wave picture. The resulting recoil ladder forms a high-dimensional qudit with programmable couplings and sufficient controllability for universal quantum computation. We demonstrate its use for analog quantum simulation, including one-dimensional curved-spacetime models and synthetic black-hole horizons, as well as for quantum information processing, where multiple logical qubits and high-fidelity gates can be realized within a single electron. In parallel, the same recoil-enabled dynamics allow the controlled creation of complex hybrid electron-photon states, in which engineered ladder transitions imprint nonclassical correlations and structure onto the emitted light. Together, these results establish recoiled free electrons as a versatile platform bridging quantum optics, quantum control, Hamiltonian engineering, quantum simulation, and quantum information processing.

DOI: 10.1103/4rv2-8jxw

I. INTRODUCTION

Free-electron quantum optics provides a powerful framework for exploring quantum light-matter interactions beyond bound electronic systems [1,2]. In this approach, swift electrons—most prominently relativistic electrons in transmission electron microscopes (TEMs)—are treated as coherent quantum waves that exchange energy and momentum with optical and electromagnetic fields. Early demonstrations of photon-induced near-field electron microscopy (PINEM) showed that free electrons can undergo coherent, phase-controlled interactions with optical fields, leading to discrete energy sidebands and optical control of electron wavefunctions [3]. Subsequent work established quantum-coherent electron-photon coupling in TEMs [4], enabling fully quantized descriptions of electron-light interactions, cavity-mediated coupling, and electron-photon entanglement [5,6].

These developments have enabled advances in ultrafast imaging [7–10], electron acceleration [11–13], and hybrid light-matter physics [14–17]. In most of these existing applications, electrons propagate in the (near-)relativistic regime, where the large electron momentum strongly suppresses quantum recoil—that is, changes to the momentum-conservation [phase-matching (PM)] condition following photon emission or absorption. As a result, free-electron quantum optics has largely been explored in a recoil-free limit.

At lower electron energies in the kiloelectron-volt range, accessible in scanning electron microscopes (SEMs), the role of recoil changes qualitatively. Free electrons can still be phase matched to optical photons, enabling strong and programmable coupling to nanophotonic and cavity structures, but photon absorption and emission now induce a measurable change in the electron momentum [18–21]. This recoil gives rise to a discrete, individually addressable ladder of electron energy states while preserving a large accessible Hilbert space. SEMs provide an attractive experimental environment for exploring this regime, offering large vacuum chambers, excellent optical access, and flexible integration with photonic structures. Recent demonstrations of PINEM and nanophotonic acceleration in SEMs highlight the feasibility and promise of this platform [22–24].

Quantum recoil in free-electron radiation has a long history, including quantum descriptions of Cherenkov and Compton emission and of free-electron amplifiers and free-electron lasers [25–29]. In these settings, photon emission or absorption changes the electron energy-momentum,

*Contact author: msirotin@g.harvard.edu
†Contact author: andrei.rasputnyi@mpl.mpg.de
‡Contact author: chloubatom@gmail.com
§Contact author: roy.shiloh@mail.huji.ac.il
‖Contact author: peter.hommelhoff@fau.de

Published by the American Physical Society under the terms of the Creative Commons Attribution 4.0 International license. Further distribution of this work must maintain attribution to the author(s) and the published article's title, journal citation, and DOI. Open access publication funded by Max Planck Society.

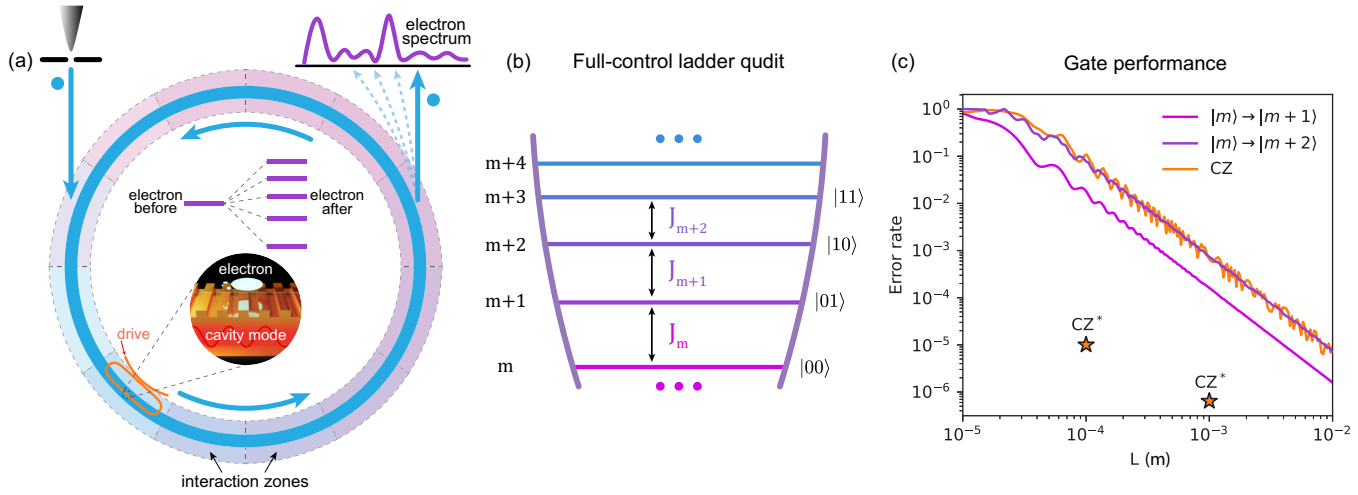


FIG. 1. Quantum simulations with a recoiled free electron. (a) Conceptual schematic of an electron undergoing cyclotron motion and sequentially interacting with multiple cavities. Inset: Electron-cavity interactions generate a synthetic anharmonic electron energy ladder, whose spectrum encodes the simulation outcome. (b) The anharmonic ladder functions as a universally controllable qudit. (c) Two qubits are encoded in four ladder levels, $|m\rangle$–$|m+3\rangle$, and gate performance (SWAP and controlled-phase, CZ) is shown as a function of interaction length per zone. See text for details.

and recoil shifts the corresponding emission and absorption resonances. The recoil considered here is the same underlying energy-momentum effect.

Rather than treating recoil as a limitation, it can be harnessed as a resource for quantum control. The recoil-induced energy ladder transforms the free electron from a passive probe into an active quantum system with a controllable internal structure in the sense of a shaped matter wave. The ladder forms an anharmonic oscillator with programmable nearest-neighbor couplings, constituting a high-dimensional ladder qudit with full and universal control. This ladder qudit enables two complementary capabilities. First, it provides a natural platform for quantum simulation, where programmable couplings realize effective lattice Hamiltonians. Using globally applied optical tones, by which we mean externally applied laser fields with specified optical frequencies, phases, and amplitudes, together with momentum-mismatch-induced selectivity, we show how one-dimensional analog black-hole Hamiltonians can be implemented, allowing simulations of curved spacetime and synthetic-horizon dynamics within a single propagating electron. Second, the same ladder qudit supports quantum information processing: Multiple logical qubits can be encoded within a single electron, and universal qudit and encoded-qubit gates can be realized using ultrafast optical control.

The same recoil-enabled dynamics also facilitate the controlled generation of nonclassical quantum states of light and hybrid light-matter states, including single-photon [30], Gottesman-Kitaev-Preskill (GKP) [31], Greenberger-Horne-Zeilinger (GHZ) [32], NOON, and squeezed-vacuum states [33–35]. Coherent energy and momentum exchange entangles the electron's ladder degrees of freedom with photonic modes, imprinting engineered quantum correlations onto the emitted light. Programmable ladder couplings allow shaping of the joint electron-photon state, enabling heralded photonic states, correlated photon emission, and structured multimode light that are difficult to generate using purely optical nonlinearities.

Starting from first principles within a relativistic quantum electrodynamics framework [36], we derive the exact interaction Hamiltonian governing the coherent coupling between free electrons and optical fields in the presence of recoil. This approach allows us to identify effective Hamiltonians describing recoil-induced ladders, programmable couplings, and nonautonomous dynamics, and to obtain exact analytical solutions in experimentally relevant limits. Together, these results establish recoiled free electrons as a powerful platform bridging quantum optics, Hamiltonian engineering, and quantum simulation with electron microscopy and quantum-enhanced sensing, enabling controlled quantum dynamics in hybrid light-matter systems.

II. QUANTUM SIMULATIONS WITH RECOILED FREE ELECTRONS

We consider the interaction of free electrons with the evanescent electric field of optical cavity structures, as illustrated schematically in Fig. 1. Free electrons generated in a transmission or scanning electron microscope (TEM or SEM), or in on-chip electron sources, are prepared at the desired kinetic energy and brought into close proximity with nanophotonic or cavity-enhanced near fields. In the presence of externally applied optical drives, the cavity supports multiple modes and optical tones, enabling strong and programmable electron-photon coupling. As the electron propagates past the cavity, it can coherently exchange energy and momentum with the optical field through near-field Cherenkov radiation [25–27,37–39] or, in the presence of a diffraction grating, through Smith-Purcell-type coupling into cavity modes [40–43]. Throughout this section, we focus on the driven regime, in which the optical field is pumped and composed of multiple controllable tones. In this limit, the interaction is

dominated by stimulated processes, and if a cavity mode is not pumped at a given tone, the corresponding spontaneous contribution can be neglected. This setting enables programmable Hamiltonian engineering and the realization of effective lattice models, including curved-spacetime and analog black-hole simulations, within a single propagating electron.

In the recoiled free-electron regime, quantum recoil—namely, the change of electron momentum following photon emission or absorption—plays a central role in the dynamics. Because momentum conservation (phase matching) must be satisfied at each interaction step, the momentum change of the electron after emitting/absorbing a photon generally forces any subsequent photon to have a different frequency. As a result, if the cavity does not support additional modes or is not driven at the corresponding frequencies, further emission is suppressed, whereas in a driven multimode cavity the electron can continue emitting photons into modes of different frequencies. In this sense, quantum recoil acts as an effective spectral filter that selects the allowed transitions (see the Supplemental Material [44] for details).

We distinguish here between energy conservation and phase matching. Energy conservation fixes the allowed change of the electron and photon energies, whereas phase matching describes the spatial accumulation of the relative phase associated with their longitudinal momenta. In the effectively one-dimensional, translationally invariant geometry considered here, longitudinal phase matching expresses the corresponding longitudinal momentum-conservation requirement for an energy-conserving transition.

At electron energies in the kiloelectron-volt range, the longitudinal motion of a free electron can be phase matched to optical photons, enabling coherent light-matter interactions while simultaneously producing resolvable recoil. This recoil-induced selectivity gives rise to a discrete ladder of electron energy states that are coherently addressable and can be coupled in a programmable manner, forming an effective synthetic lattice with a large accessible Hilbert space. The combination of strong, momentum-selective coupling and free-space propagation makes this regime particularly well suited for quantum simulation of engineered lattice Hamiltonians. Experimentally, these conditions are naturally realized in scanning electron microscopes and related electron-optical platforms, which provide long interaction lengths, excellent optical access, and flexible integration of photonic structures.

Starting from the relativistic Dirac field of the free electron coupled to the electromagnetic field and transforming to a length-propagation picture (see the Supplemental Material [44]), we obtain an exact recoil-resolved description in a basis of energy sidebands $\{|m\rangle\}$, where $|m\rangle$ denotes the electron after exchanging m photons with the optical field. The propagation coordinate z along the electron trajectory plays the role of the evolution parameter, such that the electron state $|\psi(z)\rangle$ obeys a Schrödinger equation in z (with $\hbar = 1$),

$$i\frac{d}{dz}|\psi(z)\rangle = H(z)|\psi(z)\rangle, \tag{1}$$

so hereafter, "nonautonomous" refers to explicit dependence on the evolution coordinate z, rather than on laboratory time.

In the driven (pumped) regime relevant for quantum simulation, interaction with externally applied optical tones yields an explicitly nonautonomous Hamiltonian,

$$H(z) = \sum_{m,j}[J_j\, e^{i(k_{m+1}-k_m-\varkappa_j)z}\,|m{+}1\rangle\langle m| + \text{H.c.}], \tag{2}$$

where k_m is the longitudinal electron wave vector of ladder state $|m\rangle$, $\varkappa_j$ is the wave vector of the jth applied optical tone, and J_j is the effective complex coupling coefficient induced by the jth optical tone. Each tone couples globally to all ladder transitions, while selectivity arises from the momentum mismatch $k_{m+1} - k_m - \varkappa_j$, which produces rapidly oscillating phase factors along the propagation direction z.

The coupling coefficient J_j encapsulates both the intrinsic vacuum electron-photon coupling strength and the amplitude of the applied optical field. Microscopically, one may write

$$J_j \;\propto\; g_{\text{Qu}}\,\mathcal{E}_j, \tag{3}$$

where g_{Qu} is the vacuum coupling strength [45,46] and $\mathcal{E}_j$ is the complex field amplitude of the jth tone at the electron trajectory. In the absence of an external drive, the dynamics reduce to the fully quantized vacuum-coupling regime discussed in the quantum state generation sections below.

In the high-recoil regime, where $|k_{m+1} - k_m - \varkappa_j|L \gg 1$ for all off-resonant transitions over an interaction length L, the rapidly oscillating off-resonant contributions average to zero. The dynamics then reduce to an effective autonomous tight-binding Hamiltonian,

$$H_{\text{eff}} = \sum_m J_m(|m{+}1\rangle\langle m| + |m\rangle\langle m{+}1|), \tag{4}$$

with programmable nearest-neighbor couplings J_m set by the chosen tones and their phases. As shown in the Supplemental Material [44], independent control of these couplings implies universal controllability on any finite ladder truncation, both in the qudit sense and in the Lloyd-Braunstein continuous-variable universality framework [47,48].

Figure 1 summarizes the key elements of the recoiled free-electron platform and illustrates its capabilities for quantum simulation and quantum information processing. The system is based on a free electron propagating through a sequence of engineered interaction regions, where coherent coupling to optical cavity modes induces controlled energy exchange via photon recoil.

A. Interaction geometry

Figure 1(a) shows a conceptual schematic of the platform. An electron sequentially interacts with multiple optical cavities, each defining a programmable interaction zone, corresponding to a spatial segment with independently programmable optical coupling. Photon absorption and emission induce discrete shifts in the electron's longitudinal energy, generating a synthetic anharmonic ladder of recoil sidebands. Depending on the target operation, elementary transformations—such as nearest-neighbor swaps or phase shifts—can be implemented within a single interaction zone, while more complex quantum simulations or multiqubit gate sequences require a series of interaction zones applied in succession.

These interaction zones can be arranged linearly along the electron trajectory, which is the most direct implementation

assumed by the theoretical model. A more compact possibility is to reuse one or several interaction zones by guiding the electron along a closed or resonant trajectory. The simple cyclotron geometry illustrated in Fig. 1 should, however, be regarded as a schematic example of such a repeated-pass architecture rather than as a complete electron-optical design.

For example, a 1 keV electron has a velocity of $v \simeq 0.06c$, so a cyclotron orbit with diameter 10 cm corresponds to a revolution period of $\simeq$17 ns. This timescale is compatible with fast electro-optic control and permits the optical fields to be modified between successive passages. The relative optical phases must nevertheless remain referenced to a common source throughout the gate sequence.

A magnetic field of order a few millitesla ($B \simeq 2$ mT) is sufficient to realize such an orbit, well within standard SEM capabilities. Photon recoil, however, also changes the electron trajectory. In the nonrelativistic limit, $r = p/eB$, and therefore a small energy displacement gives

$$\frac{\delta r}{r} \simeq \frac{\delta E}{2E_{\mathrm{kin}}}. \tag{5}$$

For the representative 1 keV, $r = 5$ cm orbit and a single $\simeq$1.88 eV recoil, this corresponds to $\delta r \simeq 47$ μm per ladder step. Thus different components of a recoil-ladder superposition do not exactly retrace the same orbit in a uniform magnetic field, even though the nonrelativistic cyclotron frequency is approximately energy independent. A bare uniform-field orbit therefore requires additional focusing or energy-insensitive electron optics to maintain spatial overlap with the interaction mode over repeated passages.

An experimentally demonstrated alternative is transverse electron guiding in Paul-trap-like and autoponderomotive structures [49,50]. Autoponderomotive guides have been demonstrated over a wide electron energy range, including the keV regime, and a 1 keV miniaturized guide was estimated to provide a transverse confinement frequency of approximately $2\pi \times 46$ GHz, with a matched ground-state beam width of approximately 14 nm and an opening angle of 0.4 mrad [50]. More recently, stable resonant guiding of 50 eV electrons for up to seven round trips has been experimentally demonstrated using an autoponderomotive linear electron resonator with fast switchable electron mirrors [51]; related guiding has subsequently been extended to electron energies up to 9.5 keV [52]. These results provide an experimentally motivated route for maintaining transverse confinement over repeated interactions, although they do not by themselves establish preservation of the longitudinal coherence of a recoil-ladder superposition.

Longitudinal dispersion imposes an independent constraint. For adjacent recoil states at $E_{\mathrm{kin}} = 1$ keV, $\delta v/v \simeq \delta E/(2E_{\mathrm{kin}}) \simeq 9.4 \times 10^{-4}$. Over the 10-cm-diameter orbit above, this produces an arrival-time difference of approximately 16 ps, or a longitudinal walk-off of approximately 0.3 mm, per revolution and per photon recoil. Without dispersion compensation, this walk-off accumulates over repeated passages and can eventually exceed the longitudinal extent over which the ladder components remain mutually coherent or overlap the same optical interaction. The useful number of repeated passages is therefore set by the electron energy spread, wave packet duration and coherence length, interaction-mode geometry, and electron-optical dispersion rather than by the recoil ladder itself. Energy chirping, magnetic or electrostatic dispersion compensation, and guided/resonator geometries with reduced chromatic sensitivity provide possible routes to extending this range.

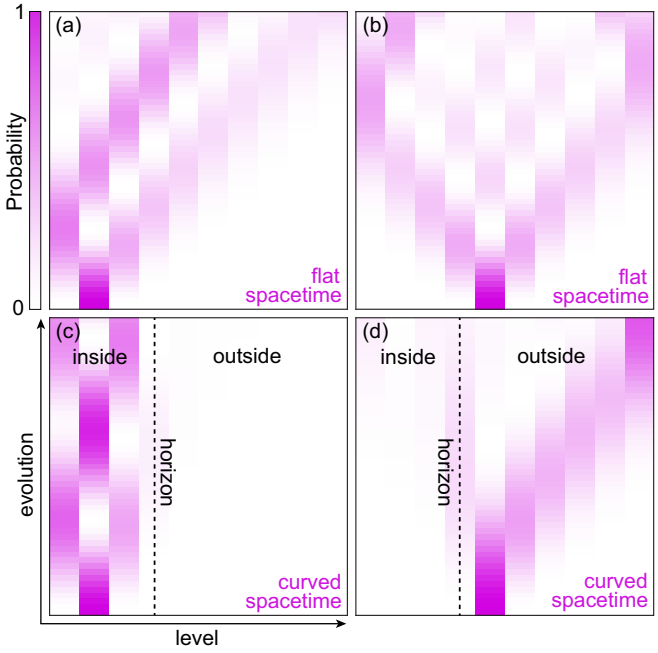


FIG. 2. Quantum walks in flat and curved spacetime. (a), (b) Quantum walk dynamics on an effective flat spacetime with uniform ladder couplings. (c), (d) Quantum walk dynamics on a curved spacetime corresponding to a one-dimensional analog black hole, with a horizon located at ladder index $m = 3$. The horizon induces asymmetric propagation: Excitations initialized inside the horizon remain trapped ($m_0 = 1$) [panel (c)], while those initialized outside propagate away ($m_0 = 4$) [panel (d).

Importantly, none of the gate or Hamiltonian-engineering calculations presented here require a closed cyclotron orbit: They require only a sequence of phase-controlled interaction zones. A linear sequence of interaction regions therefore provides the conservative architecture underlying the present theoretical proposal, while cyclotron and guided electron-resonator implementations represent possible compact repeated-pass extensions.

After completing the programmed sequence of interactions, the quantum dynamics are encoded in the electron energy spectrum, which can be read out using an electron energy spectrometer and a microchannel plate or a similar single-electron-sensitive detector.

As shown in Fig. 1(b), the recoil-induced energy ladder forms a high-dimensional qudit with full and universal control over its nearest-neighbor couplings. By programming the amplitudes, phases, and spatial arrangement of the optical drives, one can engineer a wide class of effective ladder Hamiltonians within a single propagating particle. This capability goes beyond static tight-binding models and allows the simulation of position-dependent and nonuniform coupling landscapes that emulate effective spacetime geometries (see Fig. 2 and the following discussion).

B. Quantum control

Figure 1(c) highlights the use of the ladder qudit for quantum information processing. A central advantage of the recoiled-electron platform is that a high-dimensional qudit can be encoded within a single physical system by selecting an appropriate subset of ladder states. In contrast to many naturally anharmonic bound systems, such as superconducting circuits, the free-electron energy ladder is not intrinsically restricted to a small number of bound levels and may therefore provide access to a comparatively large Hilbert space. In general, an effective register of N qubits can be embedded in a ladder qudit using 2^N energy levels. This encoding allows multiqubit operations to be implemented within a single coherent quantum object, potentially reducing the overhead associated with coupling many separate qubits. Importantly, however, the tensor-product structure of the encoded qubits is virtual rather than physical: 2^N spectrally resolved ladder states are still required, and the corresponding control, readout, spectral-range, and error-correction resources do not scale in the same manner as in an architecture composed of N independently addressable physical qubits. The relative advantages and limitations of qudit-based and conventional qubit-based architectures therefore depend on the available control resources and must be assessed for a specific implementation. Related approaches based on naturally multilevel systems have been explored experimentally and theoretically for both direct qudit computation [53,54] and the encoding of multiple virtual qubits within a single physical qudit [55–57].

In the example shown, two logical qubits are encoded using four consecutive ladder states, $|m\rangle$–$|m+3\rangle$. The figure reports the performance of both qudit-level operations and encoded-qubit gates as a function of the interaction length per zone. Elementary operations, such as a nearest-neighbor swap $\mathrm{SWAP}_{|m\rangle\to|m+1\rangle}$, can be implemented using a single interaction zone. This swap operation is native to the recoiled-electron ladder, as it directly corresponds to the fundamental nearest-neighbor coupling. As such, it provides a natural operation within the ladder and serves as a key building block for more complex gates. More elaborate transformations—such as the next-nearest-neighbor swap $\mathrm{SWAP}_{|m\rangle\to|m+2\rangle}$—are constructed from sequences of nearest-neighbor swaps and therefore require multiple interaction zones to refocus intermediate levels and suppress leakage. These swap-based operations form the backbone of universal control in the ladder qudit, enabling the compilation of arbitrary multiqubit and multilevel gates (see the Supplemental Material [44]).

A key ingredient for universal multiqubit control is the availability of high-fidelity entangling gates. As a representative example, we implement a controlled-phase gate, CZ, using two complementary approaches. In the first, a single 2π interaction involving an auxiliary ladder level $|m+4\rangle$ produces the desired conditional phase [orange curve in Fig. 1(c)]. In the second, higher-fidelity CZ operations are realized using composite pulse sequences optimized over multiple interaction zones [Fig. 1(c), stars CZ*]. Specifically, we employ optimal control over several interaction zones, while restricting the maximum length $L_{\max}$ of a single interaction zone. We optimize over seven interaction zones with $L_{\max} = 10^{-4}$ m (left star) and over nine interaction zones with $L_{\max} = 10^{-3}$ m (right star). These multizone sequences suppress residual phase errors and leakage, achieving substantially higher fidelities than simple single-zone implementations.

The dominant error mechanism in these gates arises from population leakage outside the encoded subspace. In the recoiled-electron ladder, this leakage decreases quadratically with the interaction length, leading to an overall error scaling proportional to $1/L^2$. We emphasize that the errors shown here are evaluated within the idealized coherent ladder model and therefore do not include additional experimental imperfections. In particular, uncompensated longitudinal electron-wave-packet dispersion, finite energy spread, phase fluctuations, and imperfect spatial overlap with the optical modes can further reduce the gate fidelity and limit the number of ladder states that remain coherently accessible. Increasing the interaction length or distributing the operation across multiple zones enables systematic improvement of gate fidelity within the idealized model. Together, these results demonstrate that the ladder qudit supports high-fidelity multiqubit operations with favorable scaling, making recoiled free electrons a promising platform for compact quantum information processing.

C. Analogue simulations

Beyond gate-based operations, the same programmable recoil ladder can also be used as an analog quantum simulator. To demonstrate this capability, we present an example in which the ladder dynamics emulate wave propagation in a one-dimensional curved spacetime, realizing an analog black-hole Hamiltonian with a synthetic horizon.

In this setting, the ladder index m is interpreted as a discrete synthetic spatial coordinate, while the propagation coordinate z plays the role of time for the simulated dynamics. By tailoring the optical-tone amplitudes and phases, one can engineer position-dependent hopping amplitudes along this synthetic dimension, thereby realizing effective lattice Hamiltonians that emulate wave propagation in curved spacetime.

Figure 2 illustrates this idea for a one-dimensional analog black-hole Hamiltonian associated with a Painlevé-Gullstrand metric containing a smooth Rindler horizon [58,59]. In the corresponding tight-binding description, wave packets propagate along the synthetic coordinate m. The relevant group velocity is therefore not the physical longitudinal velocity of the electron, but the effective velocity dm/dz of a wave packet in the recoil ladder, determined by the engineered band structure and coupling profile.

The analog horizon occurs at the synthetic position where the laboratory-frame group velocity of an outward-propagating mode vanishes. Equivalently, this is the point where the engineered effective flow cancels the intrinsic propagation velocity of the lattice excitation, so that modes on one side of the horizon cannot propagate back across it. Experimentally, this horizon is implemented by programming a spatially varying ladder-coupling profile, for example, through a rapid variation or sign change of the effective hopping amplitudes. In the simulations shown, the interaction length is fixed to $L = 10^{-3}$ m, and the effective evolution is generated by gradually increasing the magnitude of the applied optical couplings $|J|$.

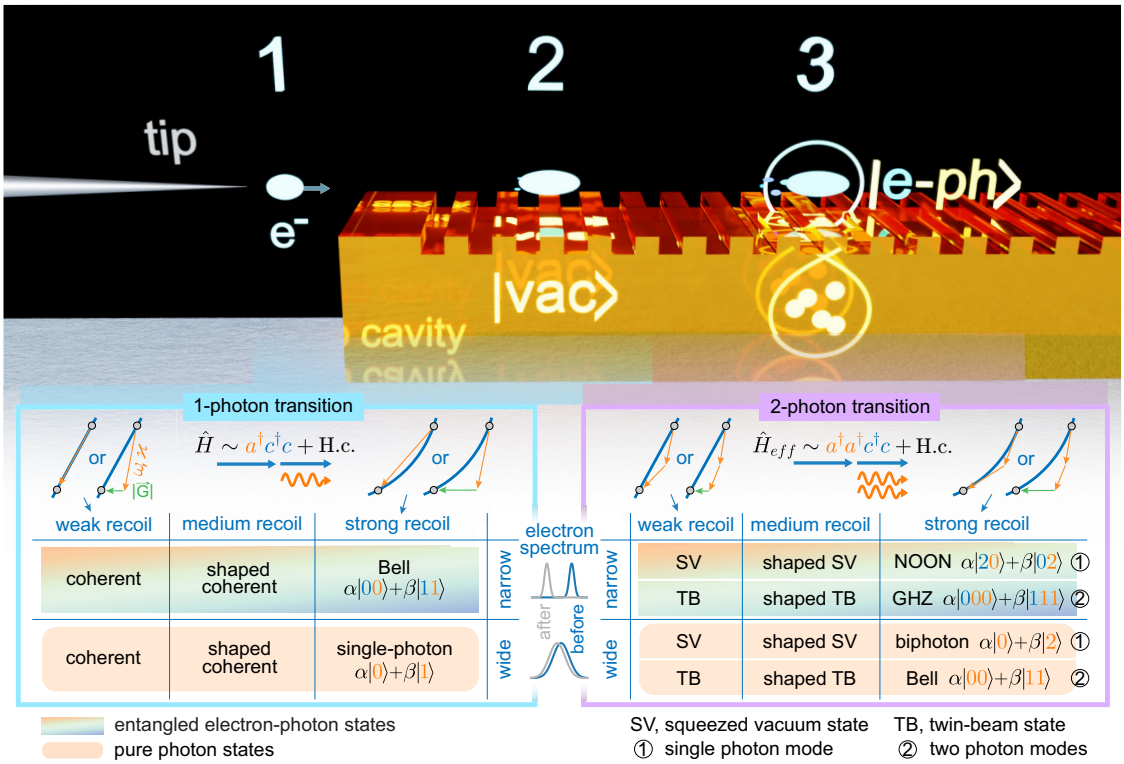


FIG. 3. Schematic summary of electron-photon state generation. (1) Free-electron emission (e.g., from a metallic nanotip). (2) Interaction with the evanescent vacuum field of an optical cavity, $|\text{vac}\rangle$. (3) Formation of an entangled electron-photon state, $|\text{e-ph}\rangle$. Depending on the interaction order (one- or two-photon), recoil strength, and electron spectral width, a variety of quantum states can be generated. The table summarizes the role of electron dispersion (linear: weak recoil; nonlinear: strong recoil) and electron spectral width (overlapping distinguishable spectra before and after interaction).

To demonstrate the resulting horizon physics, we prepare an initial excitation localized either inside or outside the effective horizon. When initialized inside the horizon, the excitation remains trapped and cannot propagate outward, reflecting the unidirectional flow imposed by the curved-spacetime geometry. In contrast, an excitation prepared outside the horizon propagates away from the black hole, demonstrating the asymmetric transport characteristic of horizon physics. This behavior directly mirrors the causal structure of black-hole spacetimes, where information inside the horizon is prevented from escaping.

The simulation is implemented using simultaneously applied optical tones, with selectivity arising from momentum mismatch in the high-recoil regime. Under these conditions, the dynamics reduce to an effective autonomous Hamiltonian H_{eff} that faithfully reproduces the desired curved-spacetime lattice model. Importantly, because the optical tones can be controlled individually and modulated on ultrafast timescales, this platform naturally enables the study of time-dependent curved-spacetime geometries, including dynamical horizons and evolving metric profiles, realized by selectively addressing different ladder levels and modulating their couplings to induce spatially varying dispersion relations with horizonlike turning points. Such rapid control provides a direct analog of cosmological particle production and dynamical Casimir-type effects [60], in which time-dependent backgrounds generate excitations from the vacuum. In this respect, the recoiled free-electron platform offers a significant advantage over superconducting-circuit implementations [59], where the achievable timescales for dynamically varying the effective metric are typically much slower. Beyond single-particle transport, the same framework supports investigations of mode conversion, horizon-induced correlations, and Hawking-like processes, providing a scalable route to analog-gravity simulations with recoiled free electrons. Full details of the black-hole Hamiltonian, coupling profiles, and numerical simulation protocol are provided in the Supplemental Material [44].

III. QUANTUM STATE GENERATION WITH RECOILED FREE ELECTRONS

We now turn to a complementary regime of the same electron-cavity system, in which the cavity is initially prepared in the vacuum state or in low-lying photon Fock states, in the absence of an external coherent drive (Fig. 3). In this case, the interaction between a flying electron and the quantized near field of an empty cavity leads to the generation of entangled electron-photon states. As the electron traverses the cavity, it may emit photons into the cavity mode or absorb photons from it, provided that the phase-matching condition between the electron momentum change and the photon momentum is satisfied (see additionally Fig. S1(a) of the Supplemental Material [44]). The nature of the resulting quantum states depends sensitively on the electron dispersion. For relativistic electrons with nearly linear dispersion,

recoil is weak and photon emission leads to approximately Poissonian statistics [45]. In contrast, for slow electrons with parabolic dispersion, quantum recoil becomes significant and suppresses consecutive emission of photons with the same frequency due to accumulated phase mismatch [18]. As a result, subsequent photon emission requires different frequencies, giving rise to nonclassical photon statistics and structured hybrid light-matter states. In the following sections, we analyze this vacuum-coupling regime in detail and show how quantum recoil enables the unit-probability generation in the ideal model ("deterministic" hereafter) of a broad class of nonclassical electron-photon and purely photonic states.

To quantitatively describe these processes, we consider a fully quantized interaction Hamiltonian of the form $H \sim g_{\mathrm{Qu}}\,\hat{a}^\dagger\hat{c}^\dagger\hat{c} + \mathrm{H.c.}$, where $\hat{c}^\dagger$ and $\hat{a}^\dagger$ are the electron and photon creation operators, respectively, and g_{Qu} is the vacuum electron-photon coupling strength. If the cavity is initially in the vacuum state $|0\rangle$ and the electron has initial energy $E_0 = \hbar\Omega_0$, the joint state can be expanded as $|\psi\rangle = \sum_{n\geqslant 0} C_{-n}|-n, n\rangle$, where $|-n, n\rangle \equiv |E_0 - n\hbar\omega\rangle \otimes |n\rangle$ denotes an electron that has lost n photons of energy $\hbar\omega$ (so $\Delta\Omega_0 = n\omega$) while the cavity occupies the n-photon Fock state $|n\rangle$. We refer to the state $|-n, n\rangle$ as the nth level of the electron-photon system. In the following, we solve this problem numerically and, in appropriate limits, obtain exact analytical solutions after autonomization, allowing for a direct comparison between the two approaches.

We introduce the PM width σ as the recoil parameter, which characterizes how many photons an electron can emit before recoil-induced phase mismatch becomes significant. We define σ as the continuous solution of $\Delta k_\sigma L/2 = \pi$, i.e., the first zero of the sinc phase-matching envelope. For electron energies well below the rest energy,

$$\sigma \;\approx\; \frac{8\pi\hbar}{\sqrt{2m_e}}\frac{E_{\mathrm{kin}}^{3/2}}{E_{\mathrm{ph}}^2 L} \;\approx\; 155\,\frac{[E_{\mathrm{kin}}\,(\mathrm{keV})]^{3/2}}{[E_{\mathrm{ph}}\,(\mathrm{eV})]^2\,L\,(\mu\mathrm{m})}, \tag{6}$$

where m_e is the electron mass, $E_{\mathrm{ph}} = \hbar\omega$ is the photon energy, L is the interaction length, and E_{kin} denotes the kinetic energy of the electron (see the Supplemental Material [44] for details).

The effective number of participating levels N_{eff} in the electron-photon system can be estimated from the number of emission ($\Delta\Omega/\omega < 0$) or absorption ($\Delta\Omega/\omega > 0$) sidebands, together with the zero-loss peak at $\Delta\Omega/\omega = 0$, as

$$\begin{aligned} N_{\mathrm{eff}} &\sim \sigma + 1, \quad && \sigma \gtrsim 1, \\ N_{\mathrm{eff}} &\to 2, && \sigma \lesssim 1. \end{aligned} \tag{7}$$

Figure 4(a) shows the PM width σ as a function of electron kinetic energy E_{kin} and photon vacuum wavelength λ. For small electron energies or short photon wavelengths, recoil rapidly drives the system away from phase matching, resulting in an effective two-level system for $\sigma < 1$. With increasing electron energy or longer wavelengths, more ladder levels become accessible, eventually approaching the infinite-ladder limit.

To characterize the photon statistics of the electron-photon state, we consider the normalized second-order correlation function at zero delay,

$$g^{(2)}(0) = \frac{\langle\hat{a}^\dagger\hat{a}^\dagger\hat{a}\hat{a}\rangle}{\langle\hat{a}^\dagger\hat{a}\rangle^2},$$

which exhibits antibunching for $g^{(2)} < 1$ (sub-Poissonian statistics), bunching for $g^{(2)} > 1$ (super-Poissonian statistics), and Poissonian statistics for $g^{(2)} = 1$. Values $g^{(2)} > 3$ correspond to superbunched emission.

A. Single-photon processes

We first consider single-photon transitions in the low-coupling regime ($g_{\mathrm{Qu}} \lesssim 0.5$). In the absence of recoil ($\sigma \gg 1$), the electron-photon state takes the form of a weak coherentlike state,

$$|\psi\rangle = \sum_{n=0}^{\infty} e^{-|g_{\mathrm{Qu}}|^2/2}\,\frac{g_{\mathrm{Qu}}^n}{\sqrt{n!}}|-n, n\rangle \equiv |\alpha^{\text{e-ph}}\rangle, \tag{8}$$

as previously reported [45]. As the recoil parameter σ decreases, recoil suppresses population of higher-energy ladder states, producing a sharp cutoff in the distribution for $n \gtrsim \sigma$. In the extreme recoil-dominated limit $\sigma \lesssim 1$, the system effectively reduces to a two-level subspace, $|\psi\rangle \approx c_0|0, 0\rangle + c_1|-1, 1\rangle$, with $c_1 \approx g_{\mathrm{Qu}}$.

The photon subsystem of this state can function as a single-photon source. As σ decreases, we observe a transition from Poissonian to sub-Poissonian photon statistics with clear antibunching ($g^{(2)} < 1$), as shown in Fig. 4(c). For experimentally realistic values of E_{kin}, E_{ph}, and L, recoil-induced antibunching can be substantial [Fig. 4(b)]. For example, at $E_{\mathrm{ph}} = 2.33$ eV (vacuum wavelength 532 nm), with 5 keV electrons and an interaction length of 0.4 mm, we obtain $\sigma \simeq 0.83$ and $g^{(2)} \simeq 0.05$, comparable in antibunching $g^{(2)}$ to state-of-the-art quantum-dot single-photon sources [61]. Figures 4(b) and 4(c) demonstrate that in the low-coupling regime the photon statistics curves collapse approximately onto σ-only dependence.

In the high-coupling regime ($g_{\mathrm{Qu}} \gtrsim 0.5$), the electron-photon dynamics become richer and depend on both σ and g_{Qu}. As σ decreases, the system evolves from the coherentlike state $|\alpha^{\text{e-ph}}\rangle$ toward a new class of recoil-shaped states, which we denote as $|\alpha^{\text{e-ph}}_{\text{shaped}}\rangle$ [Figs. 4(e) and 4(f)]. These states exhibit oscillatory behavior as a function of g_{Qu}: Population accumulates near the recoil cutoff $n \approx \sigma$, reflects from this boundary, and returns toward the zero-loss level. Increasing g_{Qu} leads to repeated oscillations with growing amplitude (see Fig. S5 of the Supplemental Material [44]).

In the strong recoil limit $\sigma \lesssim 1$, the shaped coherentlike state reduces to a Bell-like state, $|\psi\rangle = \alpha|0, 0\rangle + \beta|-1, 1\rangle$, with $\alpha = \cos(g_{\mathrm{Qu}})$ and $\beta = \sin(g_{\mathrm{Qu}})$, exhibiting clear Rabi oscillations (Figs. 4(e) and 4(f) and Fig. S9 of the Supplemental Material [44]). By tuning g_{Qu}, one can deterministically generate the single-photon state $|\psi\rangle = |-1, 1\rangle$ or the maximally entangled electron-photon Bell state $|\Phi^+\rangle = (|00\rangle + |11\rangle)/\sqrt{2}$, where the electron state $|-1\rangle$ is relabeled as $|1\rangle$ for clarity.

Depending on the values of σ and g_{Qu}, the photon subsystem of the shaped electron-photon state $|\alpha^{\text{e-ph}}_{\text{shaped}}\rangle$ can exhibit Poissonian, sub-Poissonian, or super-Poissonian statistics

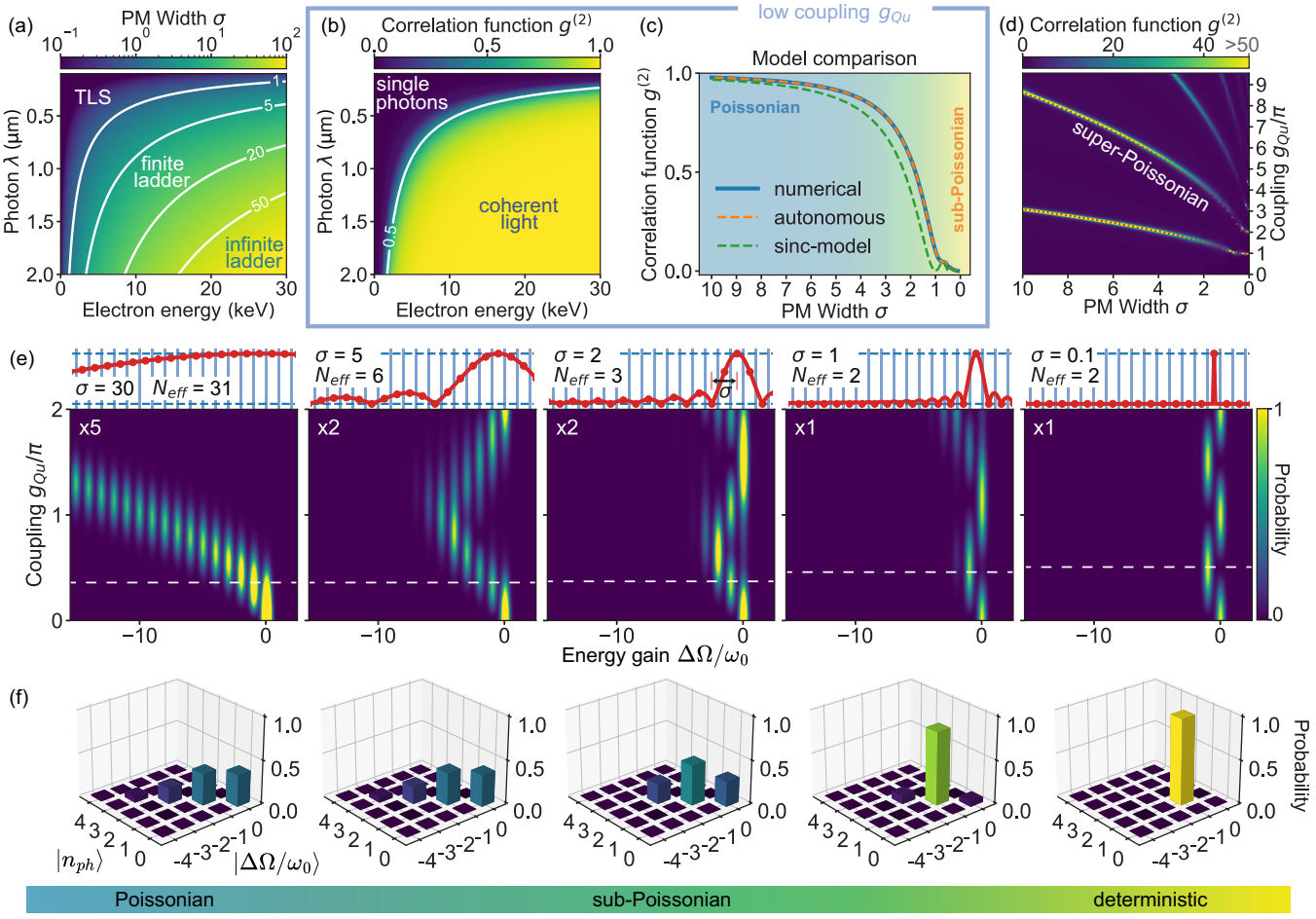


FIG. 4. Single-photon processes. (a) phase-matching width σ as a function of photon wavelength and electron energy, illustrating the transition from an infinite ladder to a finite ladder and ultimately to an effective two-level system at lower electron energies. (b) Second-order correlation function $g^{(2)}$ as a function of photon wavelength and electron energy, showing the crossover from coherent to single-photon generation. (c) Comparison of theoretical models: $g^{(2)}$ vs PM width σ, demonstrating the transition from Poissonian to sub-Poissonian statistics. (d) $g^{(2)}$ as a function of coupling strength g_{Qu} and PM width σ, revealing super-Poissonian statistics associated with multilevel Rabi oscillations. (e) Electron energy spectra for varying g_{Qu} and σ, showing the transition from Poissonian to deterministic (near-unit population transfer in the ideal model) single-photon generation (insets: relative level couplings). (f) Joint electron-photon probability distributions corresponding to the maximal single-photon generation points marked in panel (e). The interaction length is $L = 500$ μm for panels (a) and (b), and $\omega_0 \equiv \omega$. We note that $g_{\mathrm{Qu}} \gg 1$ represent theoretical large-coupling benchmarks, not the current state of the art (see the Supplemental Material [44] and Ref. [2] for details).

[Fig. 4(d)]. Pronounced peaks in the $g^{(2)}$ map coincide with revivals of the zero-loss population and correspond to the generation of superbunched k-photon states with low mean photon number $\langle \hat{N} \rangle \ll 1$ (see Fig. S5 of the Supplemental Material [44]).

Finally, we note that a free electron can act as a deterministic single-photon absorber when the cavity is initially prepared in the one-photon Fock state $|1\rangle$ (Fig. S6 of the Supplemental Material [44]). Moreover, the postinteraction electron energy spectrum provides a sensitive probe of the cavity state, allowing discrimination between Fock, coherent, and thermal photon statistics [62,63].

B. Two-photon processes

We now investigate two-photon near-field Cherenkov radiation processes (Fig. S1(f) of the Supplemental Material [44]). In this regime, single-photon emission or absorption is phase mismatched, while the simultaneous emission or absorption of two photons satisfies the phase-matching condition and therefore dominates the dynamics.

Such two-photon processes can be approximately described by an effective Hamiltonian of the form

$$H_{\mathrm{eff}} \sim g^{(2)}_{\mathrm{Qu}}\, \hat{a}^\dagger \hat{a}^\dagger \hat{c}^\dagger \hat{c} + \mathrm{H.c.},$$

where the effective two-photon coupling strength in the adiabatic-elimination regime is approximately given by

$$g^{(2)}_{\mathrm{Qu}} \equiv \frac{g^2_{\mathrm{Qu}}}{-\varphi_{-1} L}.$$

Here, $\varphi_{-1}L = -\Delta k_{-1} L = -(k(\Omega_0) - k(\Omega_{-1}) - \varkappa)L$ denotes the one-photon transition mismatch and g_{Qu} is the single-photon vacuum coupling strength. Similar to off-resonant

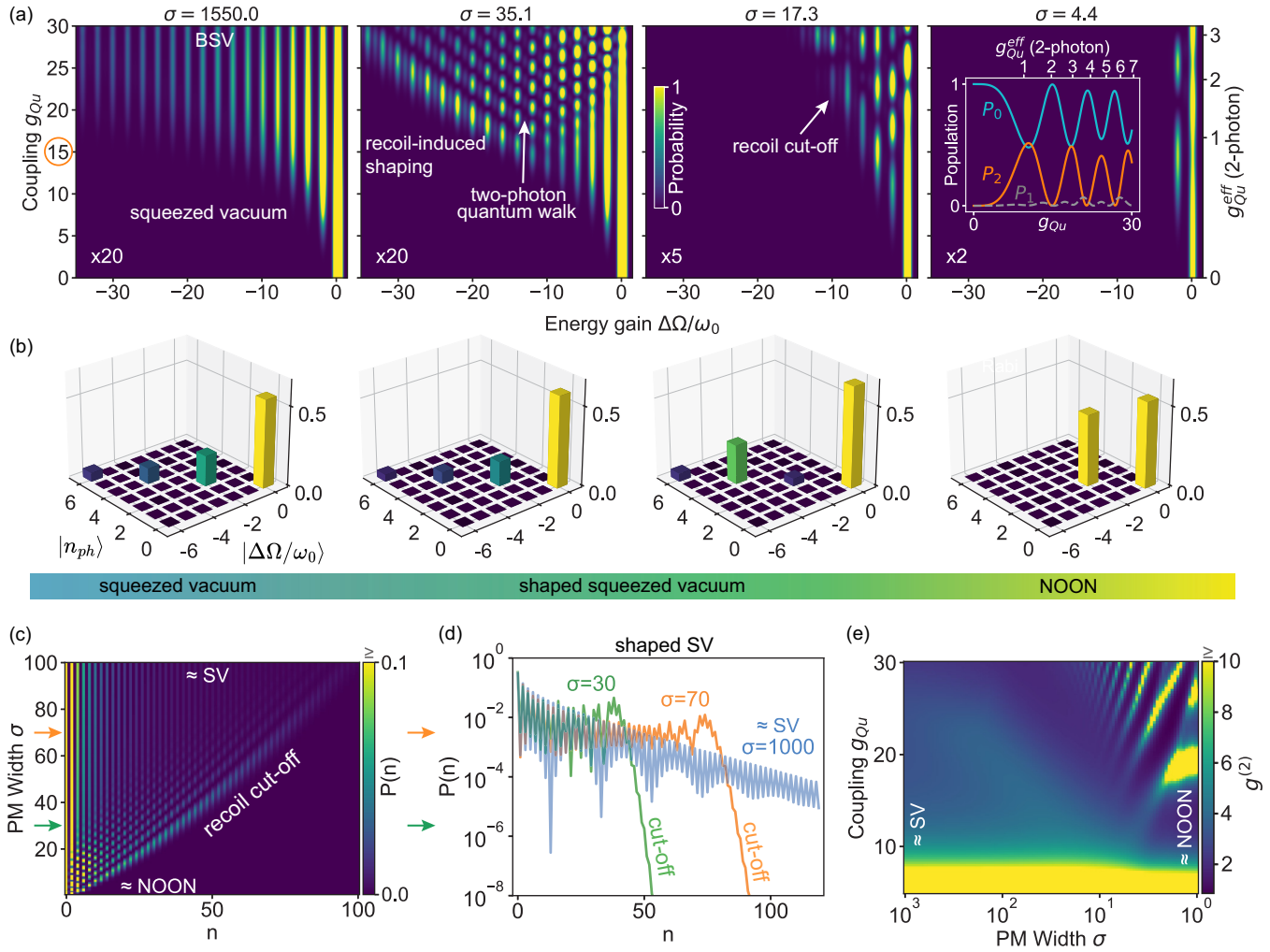


FIG. 5. Two-photon processes. (a) Electron energy spectra as a function of coupling strength g_{Qu} for different PM widths σ, showing the transition from electron-photon squeezed vacuum (SV) to recoil-shaped SV and NOON-like states (the two-photon transition is phase matched as in Fig. S1(f) of the Supplemental Material [44]). The inset shows two-photon Rabi oscillations for reduced one-photon mismatch $\varphi_{-1}L$. (b) Joint electron-photon probability distributions corresponding to the states in panel (a) for $g_{\mathrm{Qu}} = 15$. (c), (d) Photon-number distributions $P(n)$ of the electron-photon state for different σ at fixed $g_{\mathrm{Qu}} = 22$. (e) Second-order correlation function $g^{(2)}$ as a function of g_{Qu} and σ.

Raman process, the adiabatic-elimination regime occurs when single-photon coupling is strongly suppressed: $|\varphi_{-1}L| \gg |g_{\mathrm{Qu}}|\sqrt{n+1}$.

We first consider the nonrecoil regime $\sigma \gg 1$. Because the two-photon transition is phase matched, the resulting electron-photon state contains predominantly even photon numbers and even electron energy-loss states,

$$|\psi\rangle \approx c_0|0,0\rangle + c_1|{-2},2\rangle + c_2|{-4},4\rangle + \cdots .$$

We refer to this state as an electron-photon squeezed vacuum, $|\mathrm{SV}^{\text{e-ph}}\rangle$ (see the Supplemental Material [44] for details). By increasing the effective coupling $g_{\mathrm{Qu}}^{(2)}$, the system evolves from the weak photon-pair regime $|c_1| \ll |c_0|$, with $c_1 \simeq g_{\mathrm{Qu}}^{(2)}$, to a bright squeezed-vacuum state [Figs. 5(a) and 5(b), left panels]. We note that the simulation results shown are generated from the full model that includes both single- and two-photon transitions, which can be clearly seen in Fig. 5(d).

As the recoil parameter σ decreases, the electron-photon state undergoes recoil-induced shaping. We denote the resulting states as recoil-shaped squeezed vacuum, $|\mathrm{SV}^{\text{e-ph}}_{\text{shaped}}\rangle$ [Figs. 5(a) and 5(b), central panels]. Recoil suppresses population of high-n components, producing a sharp cutoff in the photon-number distribution. The position of this cutoff depends on both the coupling strength $g_{\mathrm{Qu}}^{(2)}$ [Fig. 5(a)] and the recoil parameter σ [Fig. 5(c)]. A further consequence of recoil is the emergence of a two-photon quantum walk, visible in Fig. 5(a), arising from interference of probability amplitudes reflected at the cutoff boundary.

In the strong-recoil limit $\sigma \lesssim 1$, the shaped squeezed-vacuum state reduces to a NOON-like superposition,

$$|\psi\rangle \approx \alpha|0,0\rangle + \beta|{-2},2\rangle,$$

with $\alpha = \cos(g_{\mathrm{Qu}}^{(2)})$ and $\beta = \sin(g_{\mathrm{Qu}}^{(2)})$, exhibiting two-photon Rabi oscillations (Figs. 5(a) and 5(b), and right panels and Fig. S9 of the Supplemental Material [44]). In this regime, the dynamics are well described by an effective three-level system involving the coupled states $|0,0\rangle$ and $|{-2},2\rangle$, with the intermediate state $|{-1},1\rangle$ remaining off-resonant, analogous

to a Raman process [64]. At $g^{(2)}_{\mathrm{Qu}} \simeq 1$, a maximally entangled electron-photon NOON state, $|\mathrm{NOON}\rangle = (|20\rangle + |02\rangle)/\sqrt{2}$, can be generated.

Control over σ and g_{Qu} (or equivalently, $g^{(2)}_{\mathrm{Qu}}$) enables systematic engineering of photon statistics. As shown in Figs. 5(c)–5(e), the recoil introduces a cutoff that suppresses the heavy tails characteristic of squeezed-vacuum states. In the absence of recoil ($\sigma \gg 1$), the photon statistics satisfy $g^{(2)} = 3 + 1/\langle \hat{N} \rangle$, as expected for squeezed vacuum [65]. As σ decreases, $g^{(2)}$ develops pronounced oscillatory features, allowing the degree of photon bunching to be tuned sensitively via system parameters. At the same time, both $|\mathrm{SV}^{\mathrm{e\text{-}ph}}\rangle$ and $|\mathrm{SV}^{\mathrm{e\text{-}ph}}_{\mathrm{shaped}}\rangle$ exhibit strong correlations between electron and photon subsystems, enabling photon-number resolution by measuring the electron spectrum and facilitating the preparation of non-Gaussian states of light [66].

If the cavity supports two modes that are jointly phase matched to the two-photon transition (one photon emitted into each mode), the same mechanism produces an electron-photon twin-beam state, or two-mode squeezed vacuum, $|\mathrm{Twin}^{\mathrm{e\text{-}ph}}\rangle$ (see Fig. S8 of the Supplemental Material [44]). In the strong-recoil limit $\sigma \lesssim 1$, this state evolves into a GHZ-like superposition $\alpha|000\rangle + \beta|111\rangle$ (Fig. S9 of the Supplemental Material [44]; and similar to before, the first entry represents the electron and the following two refer to the two optical modes), with the maximally entangled GHZ state $|\mathrm{GHZ}\rangle = (|000\rangle + |111\rangle)/\sqrt{2}$ obtained at $g^{(2)}_{\mathrm{Qu}} \simeq 1$. Deterministic generation of degenerate and nondegenerate photon pairs, $|\psi\rangle = |-2, 2, 0\rangle$ and $|\psi\rangle = |-2, 1, 1\rangle$, respectively, is also possible for low σ, small one-photon mismatch, and $g^{(2)}_{\mathrm{Qu}} \simeq \pi/2$ (Fig. S10(d) and S10(e) of the Supplemental Material [44]).

Finally, our framework naturally extends to one- and two-photon PINEM interactions with strong classical electromagnetic fields and recoiled electrons (Fig. S11 of the Supplemental Material [44]). Because PINEM can modulate the electron wavefunction and generate attosecond electron bunch trains [4,67–69], incorporating recoil and two-photon phase matching provides additional control knobs for electron wavefunction shaping and temporal compression. Two-photon PINEM can also lead to photon-state squeezing, analogous to ponderomotive interactions [70]. In existing PINEM experiments [71,72], the recoil parameter σ was typically much larger than the observed number of sidebands, suppressing recoil effects. PINEM in the SEM regime [22] therefore represents a promising route for the first experimental observation of recoil-induced shaping in PINEM spectra.

The present framework describes the coherent dynamics of a single electron interacting with one or several optical modes. This is the elementary description in the dilute-beam regime, where successive electrons interact independently, electron-electron interactions are negligible, and the optical mode does not retain a significant excitation from one electron to the next. A finite-current beam introduces additional effects that are not included in the present model, including Coulomb and space-charge broadening, correlations between electrons, and collective coupling when several electrons interact with the same optical mode within its coherence or storage time [15,16]. Appropriately prepared many-electron states can also produce cooperative enhancement, bunching, or superradiant dynamics. The single-electron theory developed here should therefore be regarded as the elementary building block for these more general many-electron regimes.

IV. OUTLOOK

In this work, we have investigated the role of quantum electron recoil in free-electron–photon interactions and shown that recoil fundamentally enriches the accessible quantum dynamics. We developed a first-principles quantum electrodynamics framework that treats recoil exactly and used it to reveal a recoil-induced ladder structure governed by a single dimensionless parameter σ. Within the one-dimensional coherent model considered here, the recoil strength can be conveniently characterized by the dimensionless phase-matching parameter σ, which depends only on the electron energy, photon energy, and interaction length. Together with the light-matter coupling strength, this parameter provides a compact description of the recoil-resolved dynamics studied in the present work.

This ladder structure establishes recoiled free electrons as a versatile platform for quantum simulation and Hamiltonian engineering. As demonstrated in the first part of this work, programmable couplings between recoil states enable the realization of effective lattice models within a single propagating particle, including curved-spacetime and analog black-hole Hamiltonians. In particular, we demonstrate synthetic-horizon dynamics through the asymmetric propagation of electron wave packets in an engineered recoil-space Hamiltonian. The same control framework could be extended to more complex dynamical spacetimes, nonequilibrium lattice models, and interacting quantum walks. With additional control of mode conversion and quantum correlations across the synthetic horizon, it may also enable future studies of Hawking-like pair-production processes.

Beyond quantum simulation, the same recoil-enabled dynamics provide a powerful resource for quantum state generation. Using our framework, we analyze the generation of a broad class of nonclassical joint electron-photon states and, under appropriate electron-state overlap or conditioning, purely photonic states. In particular, we propose protocols for generating electron-photon and pure-photon Bell, NOON, GHZ, squeezed-vacuum, and twin-beam states, as well as more general hybrid light-matter states enabled by recoil. Within the ideal coherent model, we further demonstrate regimes of near-unit population transfer for single-photon generation and absorption and identify recoil-enabled pathways for degenerate and nondegenerate photon-pair creation. Some of the more strongly nonclassical states explored here require larger vacuum coupling strengths and tighter experimental control than are presently established, and should therefore be viewed as targets for future strong-coupling implementations rather than as immediately available source protocols. Together, these capabilities show that the same recoil-resolved interaction can support both programmable quantum simulation and hybrid light-matter state engineering within a common theoretical framework.

The present calculations therefore establish the basic recoil-resolved control mechanisms and demonstrate their consequences within the idealized coherent model, while the

proposed protocols identify concrete directions that become accessible with increased coupling strength, improved phase stability, and more complete control of the electron and optical modes. Our work also raises several open questions for future investigation. These include the following: (1) How do squeezing processes manifest not only in the photonic subsystem, but in the electron wavefunction itself, for example, through energy-momentum correlations or quadraturelike observables; (2) how does recoil-induced squeezing modify the dynamics of cavities initially prepared in coherent or thermal states; and (3) how do recoil and multiphoton processes influence the temporal and spectral properties of attosecond electron bunches in PINEM and related schemes? On a longer timescale, the same ideas may be relevant to quantum-enhanced sensing and compact qudit-based quantum information processing, provided that the associated requirements on spectral resolution, coherent control, readout, and error correction can be met. We anticipate that the framework developed here will provide a natural starting point for addressing these questions and for assessing these prospective applications quantitatively.

Finally, because all key ingredients—electron sources, optical cavities, magnetic control, and energy-resolved detection—are naturally compatible with modern scanning electron microscopes, our approach provides a route toward experimental exploration of recoil-enabled quantum simulation and hybrid light-matter control in conventional laboratory-scale free-electron systems.

ACKNOWLEDGMENTS

This research was supported by the European Research Council Advanced Grant AccelOnChip, the Gordon and Betty Moore Foundation Grant No. 11473, and the Deutsche Forschungsgemeinschaft Project No. 429529648: TRR 306 QuCoLiMa.

M.S. and P.H. initiated the research. M.S. and A.R. derived the theory. M.S. performed the numerical calculations and wrote the first draft of the manuscript. The project was supervised by T.C., R.S., and P.H. All authors discussed the results and contributed to the writing of the manuscript.

The authors declare no competing interests.

DATA AVAILABILITY

The data supporting the findings of this study are available from the corresponding authors upon reasonable request.

[1] R. Ruimy, A. Karnieli, and I. Kaminer, Free-electron quantum optics, Nat. Phys. **21**, 193 (2025).

[2] F. J. G. de Abajo, A. Polman, C. I. Velasco, M. Kociak, L. H. G. Tizei, O. Stéphan, S. Meuret, T. Sannomiya, K. Akiba, Y. Auad, *et al.*, Roadmap for quantum nanophotonics with free electrons, ACS Photonics **12**, 4760 (2025).

[3] B. Barwick, D. J. Flannigan, and A. H. Zewail, Photon-induced near-field electron microscopy, Nature (London) **462**, 902 (2009).

[4] A. Feist, K. E. Echternkamp, J. Schauss, S. V. Yalunin, S. Schäfer, and C. Ropers, Quantum coherent optical phase modulation in an ultrafast transmission electron microscope, Nature (London) **521**, 200 (2015).

[5] A. Feist, G. Huang, G. Arend, Y. Yang, J.-W. Henke, A. S. Raja, F. J. Kappert, R. N. Wang, H. Lourenço-Martins, Z. Qiu, J. Liu, O. Kfir, T. J. Kippenberg, and C. Ropers, Cavity-mediated electron-photon pairs, Science **377**, 777 (2022).

[6] G. Huang, N. J. Engelsen, O. Kfir, C. Ropers, and T. J. Kippenberg, Electron-photon quantum state heralding using photonic integrated circuits, PRX Quantum **4**, 020351 (2023).

[7] T. Fishman, U. Haeusler, R. Dahan, M. Yannai, Y. Adiv, T. L. Abudi, R. Shiloh, O. Eyal, P. Yousefi, G. Eisenstein, P. Hommelhoff, and I. Kaminer, Imaging the field inside nanophotonic accelerators, Nat. Commun. **14**, 3687 (2023).

[8] J. H. Gaida, H. Lourenço-Martins, S. V. Yalunin, A. Feist, M. Sivis, T. Hohage, F. J. G. de Abajo, and C. Ropers, Lorentz microscopy of optical fields, Nat. Commun. **14**, 6545 (2023).

[9] T. Bucher, H. Nahari, H. Herzig Sheinfux, R. Ruimy, A. Niedermayr, R. Dahan, Q. Yan, Y. Adiv, M. Yannai, J. Chen, *et al.*, Coherently amplified ultrafast imaging using a free-electron interferometer, Nat. Photonics **18**, 809 (2024).

[10] M. C. C. Mihaila, P. Koutenský, K. Moriová, and M. Kozák, Light-based electron aberration corrector, Nat. Photonics **19**, 1309 (2025).

[11] R. J. England, R. J. Noble, K. Bane, D. H. Dowell, C.-K. Ng, J. E. Spencer, S. Tantawi, Z. Wu, R. L. Byer, E. Peralta, *et al.*, Dielectric laser accelerators, Rev. Mod. Phys. **86**, 1337 (2014).

[12] Y. Adiv, K. Wang, R. Dahan, P. Broaddus, Y. Miao, D. Black, K. Leedle, R. Byer, O. Solgaard, R. J. England, and I. Kaminer, Quantum nature of dielectric laser accelerators, Phys. Rev. X **11**, 041042 (2021).

[13] R. Shiloh, N. Schönenberger, Y. Adiv, R. Ruimy, A. Karnieli, T. Hughes, R. Joel England, K. J. Leedle, D. S. Black, Z. Zhao, P. Musumeci, R. L. Byer, A. Arie, I. Kaminer, and P. Hommelhoff, Miniature light-driven nanophotonic electron acceleration and control, Adv. Opt. Photonics **14**, 862 (2022).

[14] S. Meier, J. Heimerl, and P. Hommelhoff, Few-electron correlations after ultrafast photoemission from nanometric needle tips, Nat. Phys. **19**, 1402 (2023).

[15] R. Haindl, A. Feist, T. Domröse, M. Möller, J. H. Gaida, S. V. Yalunin, and C. Ropers, Coulomb-correlated electron number states in a transmission electron microscope beam, Nat. Phys. **19**, 1410 (2023).

[16] J. Heimerl, A. Mikhaylov, S. Meier, H. Höllerer, I. Kaminer, M. Chekhova, and P. Hommelhoff, Multiphoton electron emission with non-classical light, Nat. Phys. **20**, 945 (2024).

[17] J. Heimerl, A. Rasputnyi, J. Pölloth, S. Meier, M. Chekhova, and P. Hommelhoff, Quantum light drives electrons strongly at metal needle tips, Nat. Phys. **21**, 1899 (2025).

[18] S. Huang, R. Duan, N. Pramanik, J. S. Herrin, C. Boothroyd, Z. Liu, and L. J. Wong, Quantum recoil in free-electron interactions with atomic lattices, Nat. Photonics **17**, 224 (2023).

[19] A. Karnieli and S. Fan, Jaynes-Cummings interaction between low-energy free electrons and cavity photons, Sci. Adv. **9**, eadh2425 (2023).

[20] A. Karnieli, S. Tsesses, R. Yu, N. Rivera, A. Arie, I. Kaminer, and S. Fan, Universal and ultrafast quantum computation based on free-electron-polariton blockade, PRX Quantum **5**, 010339 (2024).

[21] A. Karnieli, C. Roques-Carmes, N. Rivera, and S. Fan, Strong coupling and single-photon nonlinearity in free-electron quantum optics, ACS Photonics **11**, 3401 (2024).

[22] R. Shiloh, T. Chlouba, and P. Hommelhoff, Quantum-coherent light-electron interaction in a scanning electron microscope, Phys. Rev. Lett. **128**, 235301 (2022).

[23] T. Chlouba, R. Shiloh, S. Kraus, L. Brückner, J. Litzel, and P. Hommelhoff, Coherent nanophotonic electron accelerator, Nature (London) **622**, 476 (2023).

[24] M. Sirotin, T. Chlouba, R. Shiloh, and P. Hommelhoff, Tunable single-photon generation in a scanning electron microscope based on silicon photonics, in *2023 Conference on Lasers and Electro-Optics Europe & European Quantum Electronics Conference (CLEO/Europe-EQEC)* (IEEE, New York, 2023), p. 1.

[25] P. A. Cherenkov, Visible emission of clean liquids by action of γ radiation, Dok. Akad. Nauk SSSR **2**, 451 (1934).

[26] V. Ginzburg, Quantum theory of radiation of electron uniformly moving in medium, Zh. Eksp. Teor. Fiz **10**, 589 (1940).

[27] V. L. Ginzburg, Radiation by uniformly moving sources (Vavilov–Cherenkov effect, transition radiation, and other phenomena), Phys. Usp. **39**, 973 (1996).

[28] R. Bonifacio, N. Piovella, G. Robb, and A. Schiavi, Quantum regime of free electron lasers starting from noise, Phys. Rev. ST Accel. Beams **9**, 090701 (2006).

[29] P. Kling, E. Giese, R. Endrich, P. Preiss, R. Sauerbrey, and W. P. Schleich, What defines the quantum regime of the free-electron laser? New J. Phys. **17**, 123019 (2015).

[30] C. Degen, F. Reinhard, and P. Cappellaro, Quantum sensing, Rev. Mod. Phys. **89**, 035002 (2017).

[31] R. Dahan, G. Baranes, A. Gorlach, R. Ruimy, N. Rivera, and I. Kaminer, Creation of optical cat and GKP states using shaped free electrons, Phys. Rev. X **13**, 031001 (2023).

[32] D. M. Greenberger, M. A. Horne, A. Shimony, and A. Zeilinger, Bell's theorem without inequalities, Am. J. Phys. **58**, 1131 (1990).

[33] K. McKenzie, N. Grosse, W. P. Bowen, S. E. Whitcomb, M. B. Gray, D. E. McClelland, and P. K. Lam, Squeezing in the audio gravitational-wave detection band, Phys. Rev. Lett. **93**, 161105 (2004).

[34] H. Grote, K. Danzmann, K. L. Dooley, R. Schnabel, J. Slutsky, and H. Vahlbruch, First long-term application of squeezed states of light in a gravitational-wave observatory, Phys. Rev. Lett. **110**, 181101 (2013).

[35] H.-S. Zhong, Y.-H. Deng, J. Qin, H. Wang, M.-C. Chen, L.-C. Peng, Y.-H. Luo, D. Wu, S.-Q. Gong, H. Su, *et al.*, Phase-programmable Gaussian boson sampling using stimulated squeezed light, Phys. Rev. Lett. **127**, 180502 (2021).

[36] C. Cohen-Tannoudji, J. Dupont-Roc, and G. Grynberg, *Photons and Atoms—Introduction to Quantum Electrodynamics* (John Wiley & Sons, Hoboken, NJ, USA, 1997).

[37] I. Tamm and I. Frank, Coherent radiation of fast electrons in a medium, Dokl. Akad. Nauk SSSR **14**, 107 (1937).

[38] I. E. Tamm, General characteristics of Vavilov-Cherenkov radiation, Science **131**, 206 (1960).

[39] Y. Adiv, H. Hu, S. Tsesses, R. Dahan, K. Wang, Y. Kurman, A. Gorlach, H. Chen, X. Lin, G. Bartal, and I. Kaminer, Observation of 2D Cherenkov radiation, Phys. Rev. X **13**, 011002 (2023).

[40] S. J. Smith and E. M. Purcell, Visible light from localized surface charges moving across a grating, Phys. Rev. **92**, 1069 (1953).

[41] G. Doucas, J. H. Mulvey, M. Omori, J. Walsh, and M. F. Kimmitt, First observation of Smith-Purcell radiation from relativistic electrons, Phys. Rev. Lett. **69**, 1761 (1992).

[42] R. Remez, N. Shapira, C. Roques-Carmes, R. Tirole, Y. Yang, Y. Lereah, M. Soljačić, I. Kaminer, and A. Arie, Spectral and spatial shaping of Smith-Purcell radiation, Phys. Rev. A **96**, 061801(R) (2017).

[43] D. Konakhovych, D. Sniezek, O. Warmusz, D. S. Black, Z. Zhao, R. J. England, and A. Szczepkowicz, Internal Smith-Purcell radiation and its interplay with Cherenkov diffraction radiation in silicon—A combined time and frequency domain numerical study, arXiv:2105.07682.

[44] See Supplemental Material at http://link.aps.org/supplemental/10.1103/4rv2-8jxw for detailed theoretical derivations, additional calculations, and discussions of the underlying assumptions, which includes Refs. [73–79].

[45] O. Kfir, Entanglements of electrons and cavity photons in the strong-coupling regime, Phys. Rev. Lett. **123**, 103602 (2019).

[46] Z. Zhao, Upper bound for the quantum coupling between free electrons and photons, Phys. Rev. Lett. **134**, 043804 (2025).

[47] S. Lloyd and S. L. Braunstein, Quantum computation over continuous variables, Phys. Rev. Lett. **82**, 1784 (1999).

[48] A. M. Eriksson, T. Sépulcre, M. Kervinen, T. Hillmann, M. Kudra, S. Dupouy, Y. Lu, M. Khanahmadi, J. Yang, C. Castillo-Moreno, P. Delsing, and S. Gasparinetti, Universal control of a bosonic mode via drive-activated native cubic interactions, Nat. Commun. **15**, 2512 (2024).

[49] J. Hoffrogge, R. Fröhlich, M. A. Kasevich, and P. Hommelhoff, Microwave guiding of electrons on a chip, Phys. Rev. Lett. **106**, 193001 (2011).

[50] R. Zimmermann, M. Seidling, and P. Hommelhoff, Charged particle guiding and beam splitting with auto-ponderomotive potentials on a chip, Nat. Commun. **12**, 390 (2021).

[51] M. Seidling, F. D. F. Schmidt-Kaler, R. Zimmermann, J. W. Simonaitis, P. D. Keathley, K. K. Berggren, and P. Hommelhoff, Resonating electrostatically guided electrons, Phys. Rev. Lett. **132**, 255001 (2024).

[52] F. Schmidt-Kaler, J. Walther, M. Seidling, R. Zimmermann, and P. Hommelhoff, Auto-ponderomotive beam guiding up to 9.5 keV, J. Vac. Sci. Technol. B **43**, 023202 (2025).

[53] E. Champion, Z. Wang, R. W. Parker, and M. S. Blok, Efficient control of a transmon qudit using effective spin-7/2 rotations, Phys. Rev. X **15**, 021096 (2025).

[54] P. Liu, R. Wang, J.-N. Zhang, Y. Zhang, X. Cai, H. Xu, Z. Li, J. Han, X. Li, G. Xue, W. Liu, L. You, Y. Jin, and H. Yu, Performing SU(d) operations and rudimentary algorithms in a superconducting transmon qudit for $d = 3$ and $d = 4$, Phys. Rev. X **13**, 021028 (2023).

[55] S. Cao, M. Bakr, G. Campanaro, S. D. Fasciati, J. Wills, D. Lall, B. Shteynas, V. Chidambaram, I. Rungger, and P. Leek, Emulating two qubits with a four-level transmon qudit for

variational quantum algorithms, Quantum Sci. Technol. **9**, 035003 (2024).

[56] A. S. Nikolaeva, E. O. Kiktenko, and A. K. Fedorov, Universal quantum computing with qubits embedded in trapped-ion qudits, Phys. Rev. A **109**, 022615 (2024).

[57] K. DeBry, N. Meister, A. Valdes Martinez, C. D. Bruzewicz, X. Shi, D. Reens, R. McConnell, I. L. Chuang, and J. Chiaverini, Error correction of a logical qubit encoded in a single atomic ion, Nat. Phys. **22**, 1446 (2026).

[58] D. Faccio, F. Belgiorno, S. Cacciatori, V. Gorini, S. Liberati, and U. Moschella, *Analogue Gravity Phenomenology: Analogue Spacetimes and Horizons, from Theory to Experiment* (Springer International Publishing, Cham, Switzerland, 2013), Vol. 870.

[59] Y.-H. Shi, R.-Q. Yang, Z. Xiang, Z.-Y. Ge, H. Li, Y.-Y. Wang, K. Huang, Y. Tian, X. Song, D. Zheng, K. Xu, R.-G. Cai, and H. Fan, Quantum simulation of Hawking radiation and curved spacetime with a superconducting on-chip black hole, Nat. Commun. **14**, 3263 (2023).

[60] J.-C. Jaskula, G. B. Partridge, M. Bonneau, R. Lopes, J. Ruaudel, D. Boiron, and C. I. Westbrook, Acoustic analog to the dynamical Casimir effect in a Bose-Einstein condensate, Phys. Rev. Lett. **109**, 220401 (2012).

[61] P. Senellart, G. Solomon, and A. White, High-performance semiconductor quantum-dot single-photon sources, Nat. Nanotechnol. **12**, 1026 (2017).

[62] R. Dahan, A. Gorlach, U. Haeusler, A. Karnieli, O. Eyal, P. Yousefi, M. Segev, A. Arie, G. Eisenstein, P. Hommelhoff, and I. Kaminer, Imprinting the quantum statistics of photons on free electrons, Science **373**, eabj7128 (2021).

[63] V. Di Giulio, M. Kociak, and F. J. G. de Abajo, Probing quantum optical excitations with fast electrons, Optica **6**, 1524 (2019).

[64] M. O. Scully and M. S. Zubairy, *Quantum Optics* (Cambridge University Press, Cambridge, 1997).

[65] D. N. Klyshko, *Photons and Nonlinear Optics* (Routledge, New York, 2017).

[66] S. Virally, P. Cusson, and D. V. Seletskiy, Enhanced electro-optic sampling with quantum probes, Phys. Rev. Lett. **127**, 270504 (2021).

[67] M. Kozák, T. Eckstein, N. Schönenberger, and P. Hommelhoff, Inelastic ponderomotive scattering of electrons at a high-intensity optical travelling wave in vacuum, Nat. Phys. **14**, 121 (2018).

[68] N. Schönenberger, A. Mittelbach, P. Yousefi, J. McNeur, U. Niedermayer, and P. Hommelhoff, Generation and characterization of attosecond microbunched electron pulse trains via dielectric laser acceleration, Phys. Rev. Lett. **123**, 264803 (2019).

[69] D. S. Black, U. Niedermayer, Y. Miao, Z. Zhao, O. Solgaard, R. L. Byer, and K. J. Leedle, Net acceleration and direct measurement of attosecond electron pulses in a silicon dielectric laser accelerator, Phys. Rev. Lett. **123**, 264802 (2019).

[70] V. Di Giulio and F. J. G. de Abajo, Optical-cavity mode squeezing by free electrons, Nanophotonics **11**, 4659 (2022).

[71] O. Kfir, H. Lourenço-Martins, G. Storeck, M. Sivis, T. R. Harvey, T. J. Kippenberg, A. Feist, and C. Ropers, Controlling free electrons with optical whispering-gallery modes, Nature (London) **582**, 46 (2020).

[72] J.-W. Henke, A. S. Raja, A. Feist, G. Huang, G. Arend, Y. Yang, F. J. Kappert, R. N. Wang, M. Möller, J. Pan, J. Liu, O. Kfir, C. Ropers, and T. J. Kippenberg, Integrated photonics enables continuous-beam electron phase modulation, Nature (London) **600**, 653 (2021).

[73] M. Eldar, Z. Chen, Y. Pan, and M. Krüger, Self-trapping of slow electrons in the energy domain, Phys. Rev. Lett. **132**, 035001 (2024).

[74] H. Levine, A. Keesling, A. Omran, H. Bernien, S. Schwartz, A. S. Zibrov, M. Endres, M. Greiner, V. Vuletić, and M. D. Lukin, High-fidelity control and entanglement of Rydberg-atom qubits, Phys. Rev. Lett. **121**, 123603 (2018).

[75] A. I. Lvovsky, Squeezed light, in *Photonics: Scientific Foundations, Technology and Applications, Volume 1*, edited by D. L. Andrews (John Wiley & Sons, Ltd., West Sussex, UK, 2015), pp. 121–163.

[76] W. Magnus, On the exponential solution of differential equations for a linear operator, Commun. Pure Appl. Math. **7**, 649 (1954).

[77] Y. Pan, B. Zhang, and D. Podolsky, Low-energy free-electron Rabi oscillation and its applications, arXiv:2304.12174.

[78] S. T. Park, M. Lin, and A. H. Zewail, Photon-induced near-field electron microscopy (PINEM): Theoretical and experimental, New J. Phys. **12**, 123028 (2010).

[79] P. R. Sharapova, G. Frascella, M. Riabinin, A. M. Pérez, O. V. Tikhonova, S. Lemieux, R. W. Boyd, G. Leuchs, and M. V. Chekhova, Properties of bright squeezed vacuum at increasing brightness, Phys. Rev. Res. **2**, 013371 (2020).